

## Article

# ZnO-ZnFe<sub>2</sub>O<sub>4</sub> Catalyst for Hydrogen Production from Methanol Steam Reforming

Bing-Zhen Hsu<sup>1,2,†</sup>, Chung-Lun Yu<sup>1,2,†</sup>, Subramanian Sakthiathan<sup>1,2</sup>, Te-Wei Chiu<sup>1,2,\*</sup>, Bing-Sheng Yu<sup>1</sup>, Chia-Cheng Lin<sup>1</sup>, Liangdong Fan<sup>3,\*</sup> and Yi-Hsuan Lee<sup>4</sup>

<sup>1</sup> Department of Materials and Mineral Resources Engineering, National Taipei University of Technology, No. 1, Section 3, Zhongxiao East Road, Taipei 106, Taiwan

<sup>2</sup> Institute of Materials Science and Engineering, National Taipei University of Technology, No. 1, Section 3, Chung-Hsiao East Road, Taipei 106, Taiwan

<sup>3</sup> Department of New Energy Science and Technology, College of Chemistry and Environmental Engineering, Shenzhen University, Shenzhen 518060, China

<sup>4</sup> Department of Mechanical Engineering, National Taipei University of Technology, No. 1, Section 3, Zhongxiao East Road, Taipei 106, Taiwan

\* Correspondence: tewe@ntut.edu.tw (T.-W.C.); fanld@szu.edu.cn (L.F.)

† These authors contributed equally to this work.

**Abstract:** In this study, ZnFe<sub>2</sub>O<sub>4</sub> and ZnO-ZnFe<sub>2</sub>O<sub>4</sub> catalysts were prepared using the glycine–nitrate process (GNP). The prepared ZnFe<sub>2</sub>O<sub>4</sub> and ZnO-ZnFe<sub>2</sub>O<sub>4</sub> catalyst powders were characterized using a scanning electron microscope, transmission electron microscope, XRD diffraction studies, and selected area diffraction pattern studies. In addition, the specific surface area was measured using a Brunauer–Emmett–Teller specific surface area analysis. The hydrogen reduction in different temperature ranges was analyzed using the H<sub>2</sub> temperature-programmed reduction technique. The specific surface area of the ZnFe<sub>2</sub>O<sub>4</sub> was 5.66 m<sup>2</sup>/g, and the specific surface area of the ZnO-ZnFe<sub>2</sub>O<sub>4</sub> was 8.20 m<sup>2</sup>/g at a G/N ratio of 1.5 and at a G/N ratio of 1.7, respectively. The specific surface area of the ZnFe<sub>2</sub>O<sub>4</sub> was 6.03 m<sup>2</sup>/g, and the specific surface area of the ZnO-ZnFe<sub>2</sub>O<sub>4</sub> was 11.67 m<sup>2</sup>/g. The ZnFe<sub>2</sub>O<sub>4</sub> and ZnO-ZnFe<sub>2</sub>O<sub>4</sub> were found to have the best catalytic effect at 500 °C. In particular, the highest H<sub>2</sub> generation rate of the ZnO-ZnFe<sub>2</sub>O<sub>4</sub> (GN = 1.7) at 500 °C was 7745 mL STP min<sup>-1</sup> g-cat<sup>-1</sup>. Moreover, the ZnO-ZnFe<sub>2</sub>O<sub>4</sub> catalyst demonstrated good H<sub>2</sub> selectivity and stability during the process of steam reforming methanol. Therefore, the ZnO-ZnFe<sub>2</sub>O<sub>4</sub> catalyst powder exhibited high catalytic activity due to the good dispersibility of the ZnO, which increased the specific surface area of the catalyst. In the future, the catalyst can be applied to the steam reforming of methanol for industrial purposes.

**Keywords:** glycine–nitrate process; ZnFe<sub>2</sub>O<sub>4</sub>; ZnO-ZnFe<sub>2</sub>O<sub>4</sub>; steam reforming of methanol; hydrogen production



**Citation:** Hsu, B.-Z.; Yu, C.-L.; Sakthiathan, S.; Chiu, T.-W.; Yu, B.-S.; Lin, C.-C.; Fan, L.; Lee, Y.-H. ZnO-ZnFe<sub>2</sub>O<sub>4</sub> Catalyst for Hydrogen Production from Methanol Steam Reforming. *Catalysts* **2023**, *13*, 762. <https://doi.org/10.3390/catal13040762>

Academic Editor: Leonarda Liotta

Received: 28 February 2023

Revised: 4 April 2023

Accepted: 13 April 2023

Published: 17 April 2023



**Copyright:** © 2023 by the authors. Licensee MDPI, Basel, Switzerland. This article is an open access article distributed under the terms and conditions of the Creative Commons Attribution (CC BY) license (<https://creativecommons.org/licenses/by/4.0/>).

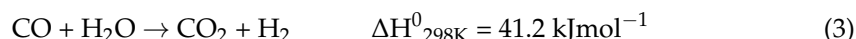
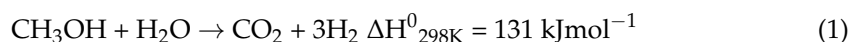
## 1. Introduction

Energy is indispensable for the rapid development of industries and daily life. Therefore, all countries consume energy uncontrollably, causing an energy crisis and the emergence of extreme global warming. Hence, alternate renewable energy sources should be developed to alleviate the energy crisis and decrease fossil fuel usage [1]. Many countries have taken measures to control the emissions of various greenhouse gases, and carbon dioxide is known to have a great impact on climate change. Although nuclear energy has excellent power generation efficiency, low carbon emissions, and a low fuel cost, it is not a completely clean and safe energy source [2]. The accident at the Fukushima Nuclear Power Plant, Japan, illustrates the dangers of nuclear power. If the radioactive materials in a nuclear power plant are released into the environment in an accident, they will cause great damage to the ecology and people. Nuclear power also presents serious problems

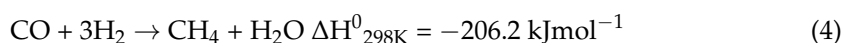
with thermal pollution and nuclear waste disposal [3,4]. Taiwan's nuclear energy industry faces rigorous challenges because the island is located at the junction of tectonic plates. As an alternative to nuclear power, many countries have actively invested in the development of two main energy sources: clean energy (non-polluting energy that produces zero carbon emissions) and alternative energy (using hydrocarbons to reduce carbon emissions) [5,6]. These two sources can provide non-toxic, clean energy for application in various fields.

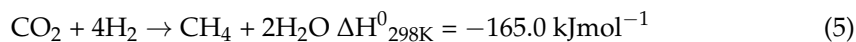
Hydrogen (H<sub>2</sub>) fuel cells are a promising technology. H<sub>2</sub> burns cleanly and produces no pollutants during combustion. In addition, H<sub>2</sub> has the greatest energy density per unit weight (i.e., 120.7 kJ g<sup>-1</sup>) when compared with other fuels [7]. In electric vehicles, hydrogen fuel cell technology provides an alternative to internal combustion engines due to its high efficiency and low carbon emissions. H<sub>2</sub> fuel cells involve a chemical reactor that can continuously provide electricity with low thermal pollution because the byproducts of the reaction are water and extremely low concentrations of pollutants such as NO<sub>x</sub> and SO<sub>x</sub> [8]. In addition, the fuel cell directly converts chemical energy without being restricted by the thermodynamic Carnot Cycle, so it achieves higher power generation efficiency. However, for the development of the hydrogen energy economy, concerns about the effective production and storage of hydrogen must be addressed.

Hydrogen–oxygen fuel cells use hydrogen as the fuel and oxygen as the oxidant [9,10]. These cells generate electricity through chemical reactions which release water vapor and heat energy. The greatest difference between fuel cells and conventional batteries is that hydrogen fuel cells do not store the electricity itself. The electrical energy is supplied by the chemical energy in the fuel. As long as there is a sustained supply of fuel, the fuel cell will persistently generate electricity [11,12]. Nevertheless, the storage of hydrogen energy presents safety issue. Therefore, the effective storage of energy is a topic that must be faced in the future. The majority of hydrogen is produced through the process of steam reforming methanol. The remaining methanol vapor converts into water and carbon dioxide. Due to the high chemical activity of methanol, steam reformation can be carried out at a lower temperature [13,14]. In addition, methanol has many advantages because it has only one carbon atom, which can greatly reduce the reaction's byproducts. Moreover, the lack of a C=C bond in the molecule means that it can be recombined at a relatively low temperature. Furthermore, methanol is preferable to other liquid sources, such as n-butane, gasoline, and petrol, for the generation of hydrogen. It is safer to handle, allows for reformation at 250 °C, has a greater H<sub>2</sub>/C ratio and no C=C bond, is low in sulfur compounds (5 ppm), and produces less coke. Therefore, methanol is regarded as one of the most advantageous sources for producing hydrogen by steam reforming [15]. Moreover, although methanol is a toxic substance, it is biodegradable. Three ways to produce hydrogen are (1) the steam reforming of methanol (SRM), (2) the methanol decomposition reaction, and (3) the water–gas shift reaction [16,17].



Conventionally, the steam reforming of methanol consists of a main reaction (the steam reforming of methanol) and several secondary reactions that occur in parallel to the main reaction. The three secondary reactions are the following reactions, namely, (2) the decomposition of methanol, (3) the water–gas shift (WGS), (4) the methanation of CO (MCO), and (5) the methanation of CO<sub>2</sub> (MCO<sub>2</sub>) [18–21].





As a result, hydrogen and carbon dioxides/carbon monoxide are obtained, and the ratio of the products depends on the process conditions or catalyst. Therefore, reducing the amount of carbon monoxide is a critical issue because it could poison the anode catalyst of the fuel cell. Hence, the selection and development of a new SRM reaction catalyst are of great importance for the stable use of fuel cells in the future. In the prior SRM reactions, copper-based catalysts with high activity and selectivity were usually used [22]. However, copper-based catalysts have two fatal disadvantages. They are susceptible to temperature fluctuations and cause a rapid loss of activity when exposed to air. Therefore, the catalytic efficiency is reduced after use. To solve the above-mentioned problems, metal-oxide-based catalysts such as  $\text{Al}_2\text{O}_3$ ,  $\text{ZnO}/\text{Al}_2\text{O}_3$ ,  $\text{ZrO}_2/\text{Al}_2\text{O}_3$ ,  $\text{CuO}/\text{ZnO}/\text{Al}_2\text{O}_3$ ,  $\text{Cr}_2\text{O}_3/\text{Al}_2\text{O}_3$ ,  $\text{Cu}/\text{ZnO}/\text{Al}_2\text{O}_3/\text{CeO}_2/\text{ZrO}_2$ ,  $\text{ZnO}$ ,  $\text{ZrO}_2$ , and  $\text{Al}_2\text{O}_3$  have been used for the MSR process due to their activity and thermal stability [23–28]. Furthermore, regarding the toxic byproduct of CO, aqueous phase reforming (APR) has the advantage of almost eliminating the CO effluent due to an in situ water–gas shift, which could improve the process [29,30].

The delafossite copper oxides  $\text{CuCrO}_2$  [31] and  $\text{CuFeO}_2$  [32] have also been used as catalysts in the SRM process. Nevertheless, the use of copper-based SRM catalysts presents difficulties in dispersibility and thermal stability, resulting in narrow ranges of the catalysis time and reaction temperature. In the literature, it was found that the copper–iron or spinel structure provides the composite with high catalytic performance and good thermal stability. Preparing a porous powder with the glycine combustion method can increase the surface area. The higher-surface-area characteristics of  $\text{ZnO}$  improve dispersibility and reduce the formation of the toxic byproduct CO [33–38]. On the other hand,  $\text{ZnO}$  and  $\text{ZnFe}_2\text{O}_4$  combine, revealing some synergistic effect. M. S. AlSalhi et al. reported that  $\text{ZnO}-\text{ZnFe}_2\text{O}_4$  formed a hybrid nanocomposite that enhanced the transfer and separation of charges, resulting in the improved catalytic performance of heterostructure photocatalysts under visible light [39]. Furthermore, the incorporation of  $\text{ZnFe}_2\text{O}_4$  into  $\text{ZnO}$  extends the range of its absorption wavelength, especially in the visible and near-infrared regions, which show a high solar utilization efficiency and photovoltaic conversion efficiency for  $\text{ZnO}-\text{ZnFe}_2\text{O}_4$  [40,41]. Moreover, the high activity and thermal stability of  $\text{ZnFe}_2\text{O}_4$  increase the catalyst's lifetime [42].  $\text{ZnO}-\text{ZnFe}_2\text{O}_4$  catalyst powder has been produced and studied to determine whether there was a synergistic effect and to achieve the best catalytic result. Therefore,  $\text{ZnO}-\text{ZnFe}_2\text{O}_4$  is used as a catalyst and effectively improves the life cycle of the SRM catalyst.

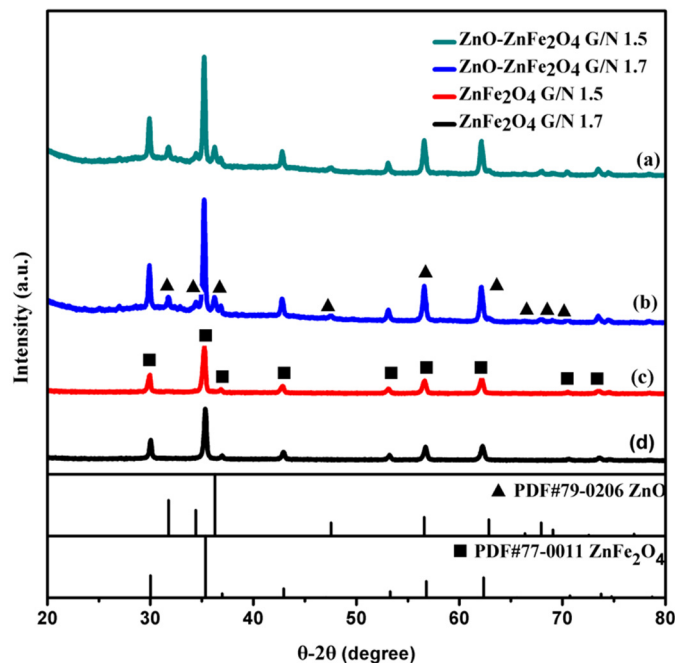
In this study, the self-combustion GNP was utilized to generate  $\text{ZnFe}_2\text{O}_4$  and  $\text{ZnO}-\text{ZnFe}_2\text{O}_4$  catalysts, which were then used for SRM. During the SRM process, the  $\text{ZnO}-\text{ZnFe}_2\text{O}_4$  (GN = 1.7) catalysts showed a high rate of hydrogen production and a low rate of coke formation. In addition, at various temperatures, the hydrogen production rates of the  $\text{ZnO}-\text{ZnFe}_2\text{O}_4$  were compared to those of  $\text{CuCrO}_2$ ,  $\text{CuFeO}_2$ , and conventional  $\text{Cu}/\text{Al}/\text{Zn}$  catalysts.

## 2. Results and Analysis

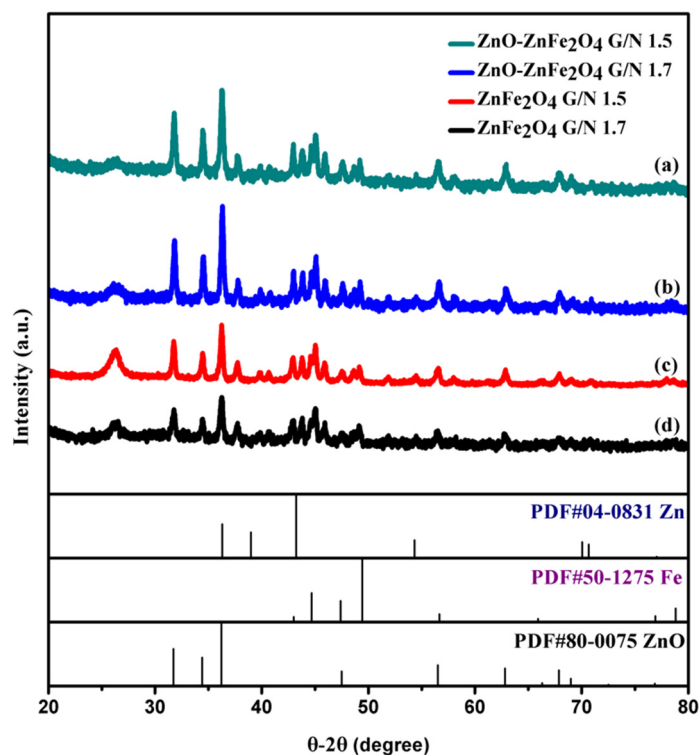
### 2.1. XRD Analysis

Figure 1a–d present the XRD diffraction patterns of  $\text{ZnFe}_2\text{O}_4$  and  $\text{ZnO}-\text{ZnFe}_2\text{O}_4$  catalyst powders with different G/N ratios (1.5 and 1.7) that were prepared by the GNP. For  $\text{ZnFe}_2\text{O}_4$ , the XRD pattern showed diffraction peaks at  $30.0^\circ$ ,  $35.3^\circ$ ,  $36.9^\circ$ ,  $42.9^\circ$ ,  $53.2^\circ$ ,  $56.7^\circ$ ,  $62.3^\circ$ ,  $70.7^\circ$ , and  $74.7^\circ$ , corresponding to the (220), (311), (222), (400), (422), (511), (440), (620), and (622) planes (PDF#77-0011). However, for  $\text{ZnO}$ , the diffraction peaks were at  $31.7^\circ$ ,  $34.4^\circ$ ,  $36.2^\circ$ ,  $47.5^\circ$ ,  $56.5^\circ$ ,  $62.8^\circ$ ,  $67.9^\circ$ ,  $69.0^\circ$ , and  $72.5^\circ$ , corresponding to the (100), (002), (101), (102), (110), (103), (200), (112), and (201) planes. In the XRD pattern, there were no impurities, such as  $\text{Fe}_2\text{O}_3$ . When the G/N ratio of the  $\text{ZnFe}_2\text{O}_4$  and  $\text{ZnO}-\text{ZnFe}_2\text{O}_4$  was 1.5, the XRD diffraction intensity was stronger than 1.7. Figure 2a–d shows that after the

SRM reaction, Zn, Fe, and ZnO appeared in the XRD diffraction analysis, indicating that Zn, Fe, and ZnO particles grew on the surface of the catalyst during the SRM process. Notably, the ZnO particle growth increased the specific surface area of the ZnO-ZnFe<sub>2</sub>O<sub>4</sub> catalyst.



**Figure 1.** XRD patterns of (a) ZnO-ZnFe<sub>2</sub>O<sub>4</sub> G/N 1.5, (b) ZnO-ZnFe<sub>2</sub>O<sub>4</sub> G/N 1.7, (c) ZnFe<sub>2</sub>O<sub>4</sub> G/N 1.5, and (d) ZnFe<sub>2</sub>O<sub>4</sub> G/N 1.7 powders obtained by the GNP.



**Figure 2.** XRD patterns of (a) ZnO-ZnFe<sub>2</sub>O<sub>4</sub> (G/N 1.5), (b) ZnO-ZnFe<sub>2</sub>O<sub>4</sub> (G/N 1.7), (c) ZnFe<sub>2</sub>O<sub>4</sub> (G/N 1.5), (d) ZnFe<sub>2</sub>O<sub>4</sub> (G/N 1.7) powders prepared by the GNP with different G/N ratios after the steam reforming process.

## 2.2. SEM and TEM Studies

FESEM studies was used to characterize the morphology and porous structures of the  $\text{ZnFe}_2\text{O}_4$  and  $\text{ZnO-ZnFe}_2\text{O}_4$  catalyst powders. Figure 3 presents FESEM images of the (a,b)  $\text{ZnFe}_2\text{O}_4$  (G/N 1.5); (c,d)  $\text{ZnFe}_2\text{O}_4$  (G/N 1.7); (e,f)  $\text{ZnO-ZnFe}_2\text{O}_4$  (G/N 1.5); (g,h)  $\text{ZnO-ZnFe}_2\text{O}_4$  (G/N 1.7) catalyst powders prepared by the GNP. Before the methanol reduction reaction, the  $\text{ZnFe}_2\text{O}_4$  and  $\text{ZnO-ZnFe}_2\text{O}_4$  catalyst powders (G/N 1.5, 1.7) had sponge-like, porous structures. Due to the rapid release and expansion of the gas during the reaction, the samples featured numerous holes of different sizes. In addition, in Figure 3a–h, a slight difference between the  $\text{ZnFe}_2\text{O}_4$  and  $\text{ZnO-ZnFe}_2\text{O}_4$  can be observed, as hexagonal  $\text{ZnO}$  grains are visible on the  $\text{ZnO-ZnFe}_2\text{O}_4$  surface.

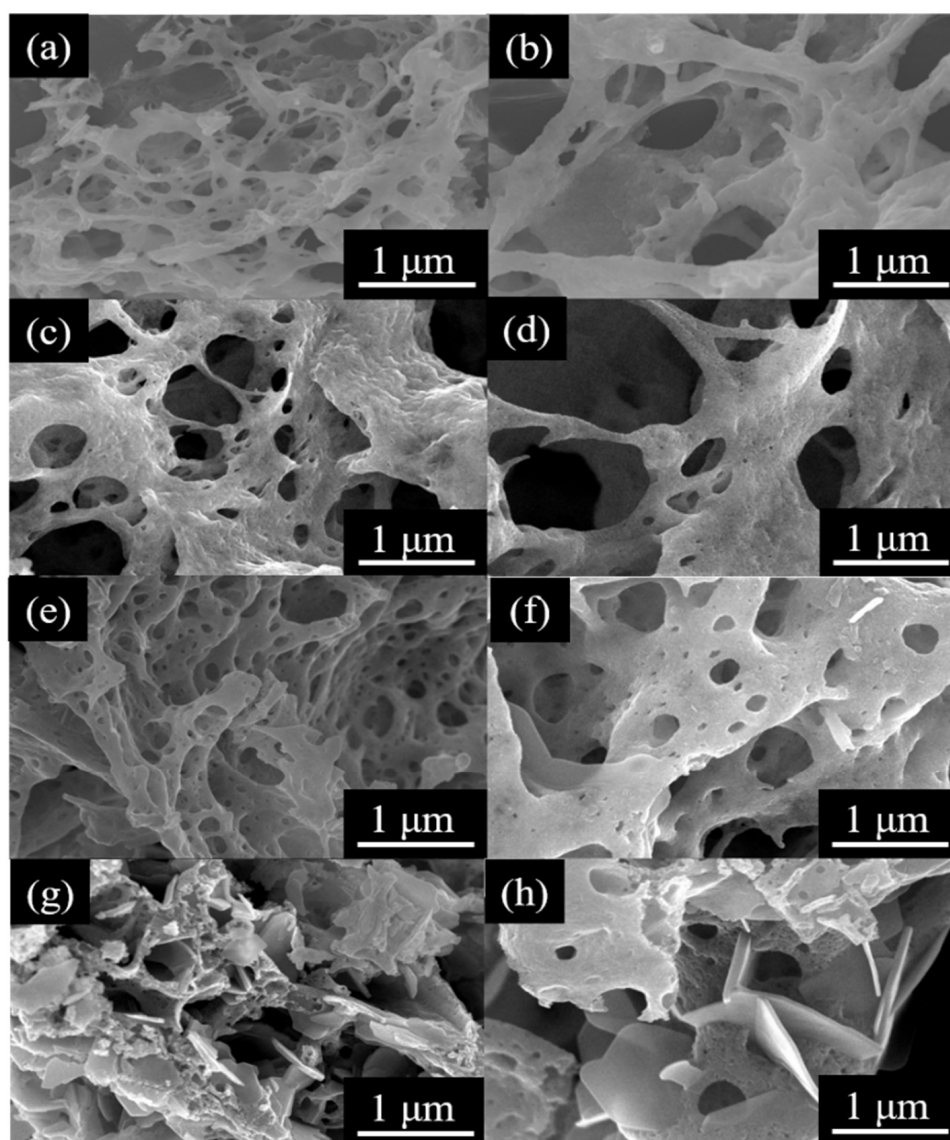


**Figure 3.** FESEM images of (a,b)  $\text{ZnFe}_2\text{O}_4$  (G/N 1.5); (c,d)  $\text{ZnFe}_2\text{O}_4$  (G/N 1.7); (e,f)  $\text{ZnO-ZnFe}_2\text{O}_4$  (G/N 1.5); (g,h)  $\text{ZnO-ZnFe}_2\text{O}_4$  (G/N 1.7) powders prepared by the GNP.

Figure 4 presents FESEM images of the (a,b)  $\text{ZnFe}_2\text{O}_4$  (G/N 1.5); (c,d)  $\text{ZnFe}_2\text{O}_4$  (G/N 1.7); (e,f)  $\text{ZnO-ZnFe}_2\text{O}_4$  (G/N 1.5); (g,h)  $\text{ZnO-ZnFe}_2\text{O}_4$  (G/N 1.7) powders after the SRM process. The images revealed that Zn and Fe particles were precipitated on the surface due to the  $\text{H}_2$  produced during the SRM reaction. XRD analysis revealed that the particles were Zn and Fe. To observe the microstructures of the  $\text{ZnFe}_2\text{O}_4$  and  $\text{ZnO-ZnFe}_2\text{O}_4$  catalyst powders at a high magnification, a TEM with 200 kV was used. Figure 5a,b present the TEM

and HRTEM images of the  $\text{ZnFe}_2\text{O}_4$ . It can be seen from the images that many irregularly shaped holes were present in the microstructure. This resulted from the significant amount of gas that was emitted during the explosion of the GNP. The interplanar spacing from the cross-section of the  $\text{ZnFe}_2\text{O}_4$  nanoparticles was approximately 4.896 Å.

A CaRIne simulation of the  $\text{ZnFe}_2\text{O}_4$  crystal and the diffraction of the selected area was performed. Figure 6a shows the selected area diffraction pattern (SAED) of the as-prepared  $\text{ZnFe}_2\text{O}_4$  powder, and Figure 6b shows the simulated diffraction pattern of the  $\text{ZnFe}_2\text{O}_4$ . The diffraction patterns in the selected area diffraction of the  $\text{ZnFe}_2\text{O}_4$  crystal corresponded to the (044), (404), and (440) diffraction patterns of  $\text{ZnFe}_2\text{O}_4$  (PDF#77-0011). The plane spacing was 4.896 Å, and the zone axis was  $[1\bar{1}1]$ . The SAED matched the XRD, which confirmed the crystal structure of the as-prepared  $\text{ZnFe}_2\text{O}_4$  powder. These results showed that the  $\text{ZnFe}_2\text{O}_4$  was a well-crystallized, single-phase arrangement of the  $[1\bar{1}1]$  pattern.

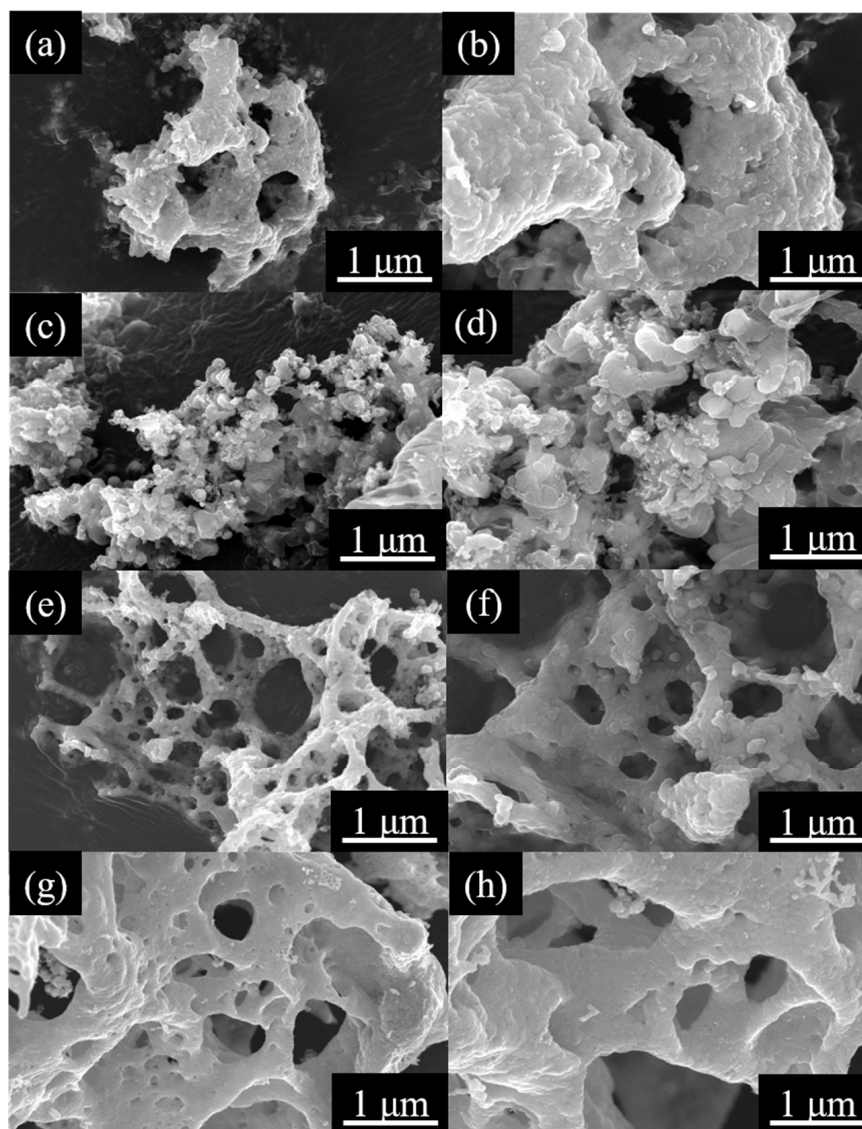


**Figure 4.** FESEM images of (a,b)  $\text{ZnFe}_2\text{O}_4$  (G/N 1.5); (c,d)  $\text{ZnFe}_2\text{O}_4$  (G/N 1.7); (e,f)  $\text{ZnO-ZnFe}_2\text{O}_4$  (G/N 1.5); (g,h)  $\text{ZnO-ZnFe}_2\text{O}_4$  (G/N 1.7) powders prepared by the GNP after the reduction at 500 °C.

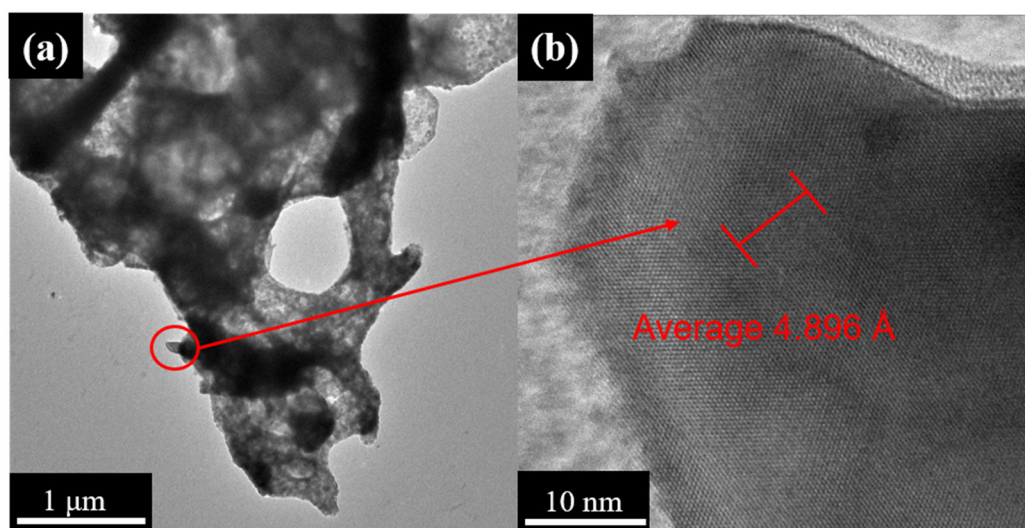


Figure 5. TEM images of  $\text{ZnFe}_2\text{O}_4$  powders: (a) TEM image; (b) HRTEM image.

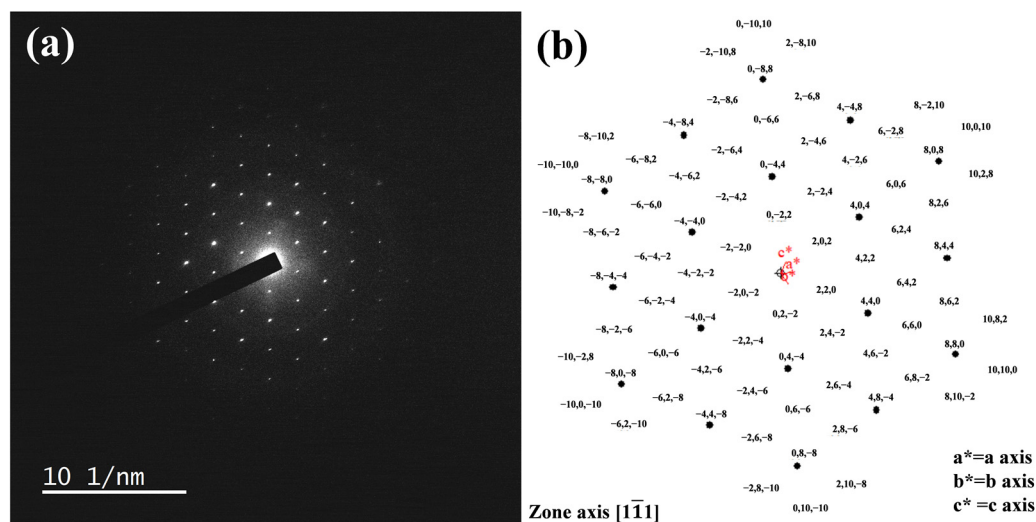
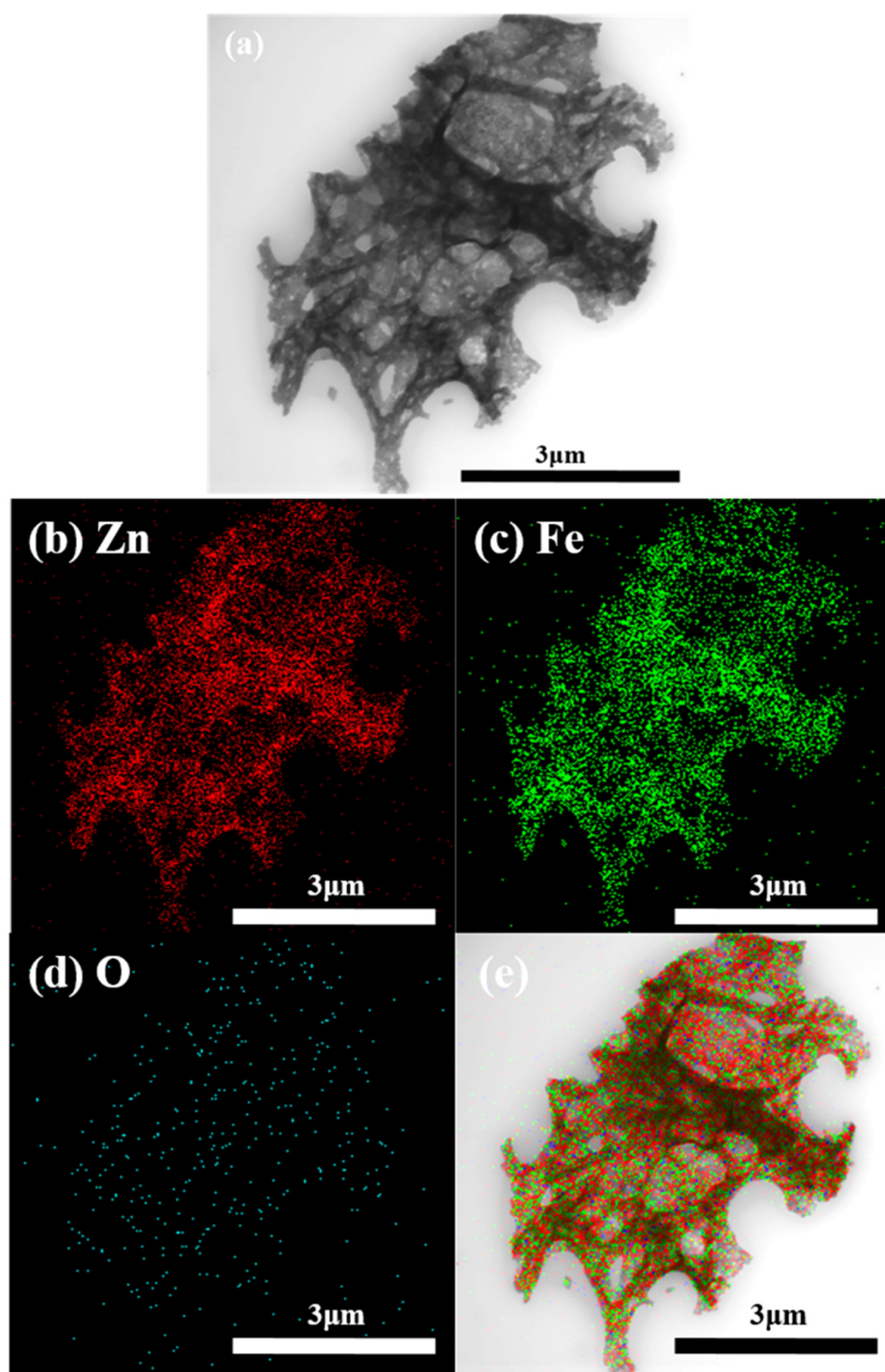


Figure 6. (a) TEM/SAED diffraction pattern image of  $\text{ZnFe}_2\text{O}_4$  powder and (b) simulated diffraction pattern of  $\text{ZnFe}_2\text{O}_4$ .

### 2.3. STEM-EDX Spectrum

The  $\text{ZnFe}_2\text{O}_4$  and  $\text{ZnO-ZnFe}_2\text{O}_4$  catalysts were analyzed by TEM-EDS mapping, which exhibited the distribution of the elements. The results are shown in Figures 7a–e and 8a–e. The elemental mapping results for the three elements showed clear, well-distributed areas. To confirm the presence of  $\text{ZnO}$  in the  $\text{ZnO-ZnFe}_2\text{O}_4$  catalyst, Figure 8 shows the STEM-EDS image and the elemental mapping of the  $\text{ZnO-ZnFe}_2\text{O}_4$  catalyst powder. From the EDS observation, it was possible to find areas that did not contain Fe. Thus, it could be inferred that  $\text{ZnO}$  was present. Figure 9 presents the STEM elemental mapping images of the  $\text{ZnO-ZnFe}_2\text{O}_4$  catalyst after reduction at  $500^\circ\text{C}$ , showing that Zn, Fe, and  $\text{ZnO}$  particles had precipitated.



**Figure 7.** STEM-EDS image and elemental mapping of ZnFe<sub>2</sub>O<sub>4</sub> powder prepared by the GNP: (a) STEM image, (b) Zn, (c) Fe, (d) O, and (e) elemental mapping of Zn, Fe, and O overlap.

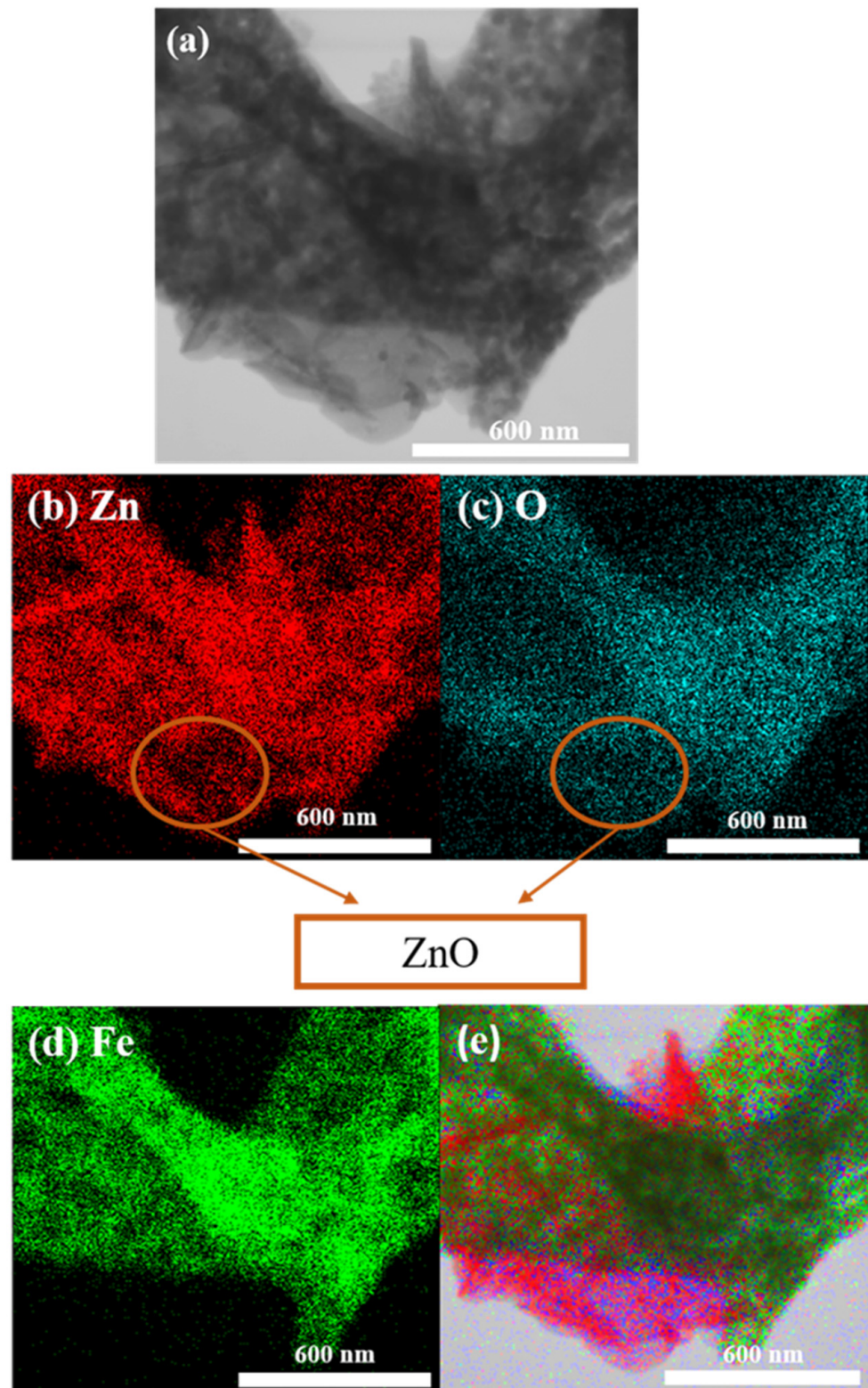


**Figure 8.** STEM-EDS image and elemental mapping of ZnO-ZnFe<sub>2</sub>O<sub>4</sub> catalyst powder prepared by the GNP: (a) STEM image, (b) Zn, (c) O, (d) Fe, and (e) elemental mapping of Zn, Fe, and O overlap.

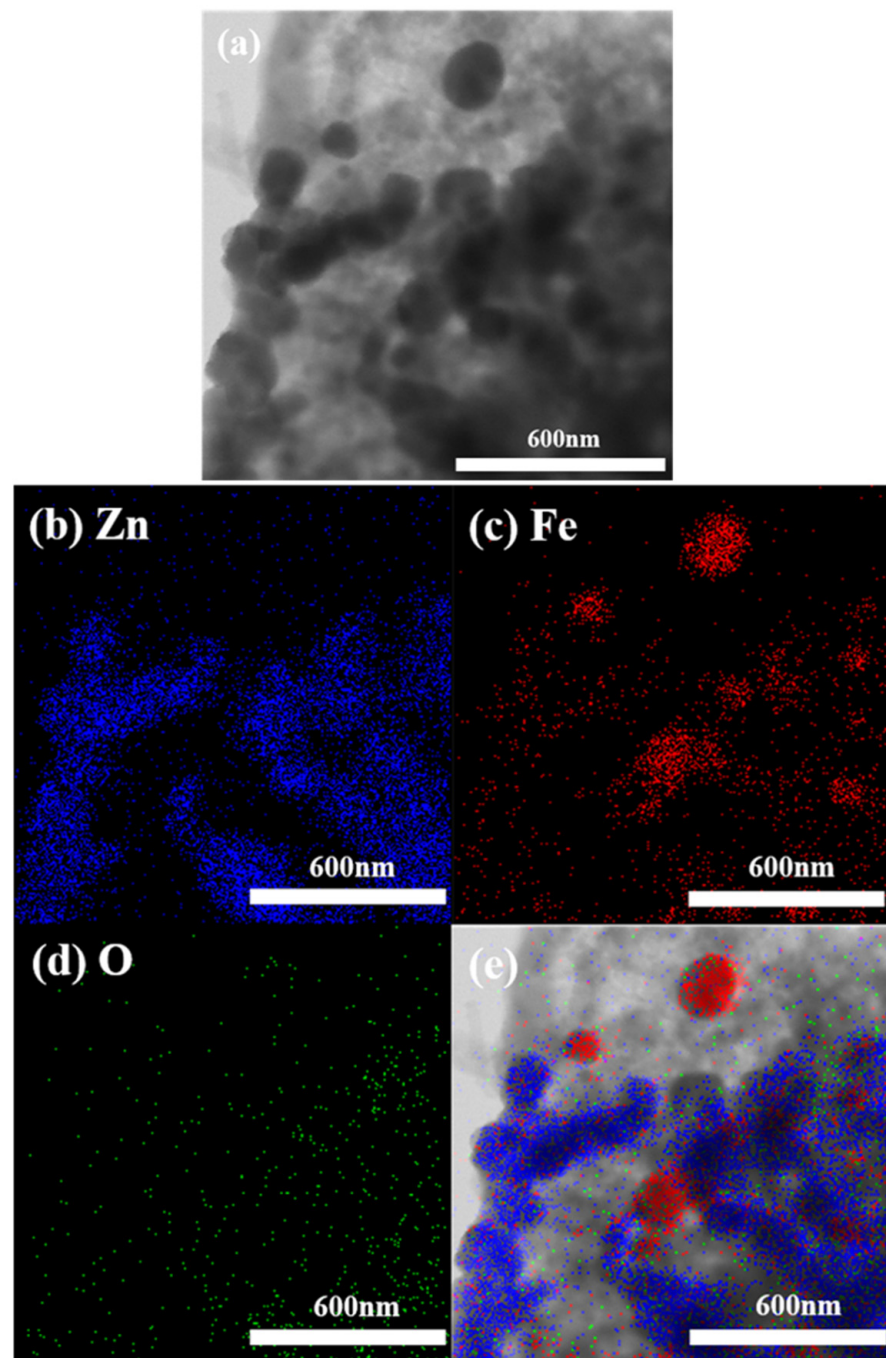


**Figure 9.** STEM elemental mapping images of the ZnO-ZnFe<sub>2</sub>O<sub>4</sub> catalyst after reduction at 500 °C: (a) STEM image, (b) Zn, (c) Fe, (d) O, and (e) elemental mapping of Zn, Fe, and O.

#### 2.4. BET Analysis

The specific surface area of the powder affects the catalytic ability. Therefore, a BET analysis was used to determine whether the powder had a high specific surface area. Table 1 shows that ZnFe<sub>2</sub>O<sub>4</sub> and ZnO-ZnFe<sub>2</sub>O<sub>4</sub> (G/N = 1.5) had lower surface areas. Further, the ZnFe<sub>2</sub>O<sub>4</sub> and ZnO-ZnFe<sub>2</sub>O<sub>4</sub> (G/N = 1.7) catalyst powders had the largest specific surface areas of 6.03 and 11.67 m<sup>2</sup>/g, respectively. Here, the G/N ratio was not affected by the surface area of the ZnFe<sub>2</sub>O<sub>4</sub> and ZnO-ZnFe<sub>2</sub>O<sub>4</sub>. In the ZnFe<sub>2</sub>O<sub>4</sub> powder combined with ZnO, the specific surface area was significantly improved, as ZnO could effectively increase the dispersion of the catalyst and strengthen the catalytic activity. Figure 10a–d shows the N<sub>2</sub> adsorption/desorption curves and  $\epsilon$  the pore size distributions of the ZnFe<sub>2</sub>O<sub>4</sub>

and ZnO-ZnFe<sub>2</sub>O<sub>4</sub> catalyst powders prepared by the GNP. There were six types of curves for N<sub>2</sub> adsorption/desorption. It can be seen from the analysis that the ZnFe<sub>2</sub>O<sub>4</sub> and ZnO-ZnFe<sub>2</sub>O<sub>4</sub> catalysts belonged to the fourth type. Hysteresis loops were more common in the fourth type of adsorption isotherms. Catalyst powder prepared by the GNP had an H<sub>3</sub>-type hysteresis loop isotherm. There was no obvious saturated adsorption plateau, indicating that the pore structure was very irregular. This also confirmed the irregular hole shapes in the SEM images. Adsorption saturation was not exhibited in the higher relative pressure region. The ZnFe<sub>2</sub>O<sub>4</sub> and ZnO-ZnFe<sub>2</sub>O<sub>4</sub> catalysts had large pore size distributions of approximately 16.71 nm (Figure 10e). In addition, the presence of ZnO and the different GN ratios did not affect the pore size distribution.

**Table 1.** The surface areas of the GNP-prepared ZnFe<sub>2</sub>O<sub>4</sub> and ZnO-ZnFe<sub>2</sub>O<sub>4</sub> catalyst powders.

Sample	Specific Surface Area (m <sup>2</sup> /g)
ZnFe <sub>2</sub> O <sub>4</sub> (G/N 1.5)	5.66
ZnFe <sub>2</sub> O <sub>4</sub> (G/N 1.7)	6.03
ZnO-ZnFe <sub>2</sub> O <sub>4</sub> (G/N 1.5)	8.20
ZnO-ZnFe <sub>2</sub> O <sub>4</sub> (G/N 1.7)	11.67

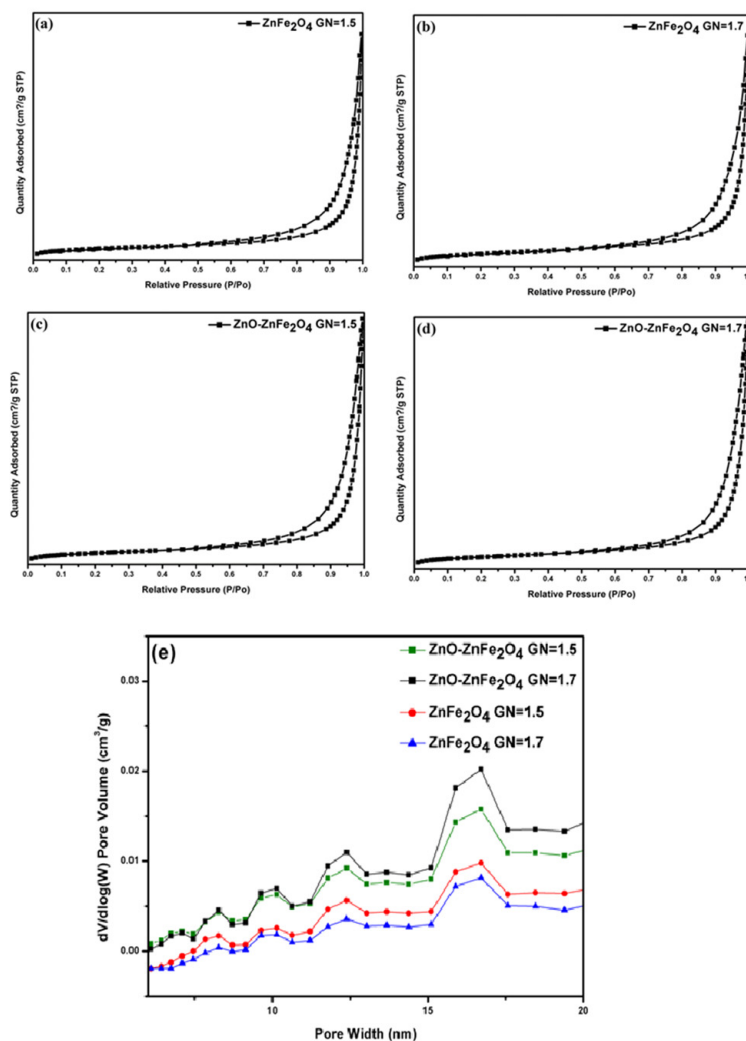


**Figure 10.** (a–d) N<sub>2</sub> adsorption/desorption curves and (e) pore size distribution of ZnFe<sub>2</sub>O<sub>4</sub> and ZnO-ZnFe<sub>2</sub>O<sub>4</sub> catalyst powder prepared by the GNP.

### 2.5. H<sub>2</sub>-TPR Analysis

The reduction behaviors of the ZnFe<sub>2</sub>O<sub>4</sub> and ZnO-ZnFe<sub>2</sub>O<sub>4</sub>, examined by TPR, are shown in Figure 11, which presents the H<sub>2</sub>-TPR profiles of (a) ZnFe<sub>2</sub>O<sub>4</sub> (GN = 1.5), (b) ZnFe<sub>2</sub>O<sub>4</sub> (GN = 1.7), (c) ZnO-ZnFe<sub>2</sub>O<sub>4</sub> (GN = 1.5), and (d) ZnO-ZnFe<sub>2</sub>O<sub>4</sub> (GN = 1.7). According to the literature, ZnO was reduced between 400 °C and 600 °C, showing a flat peak instead of a sharp peak [43,44]. There were three modes of the Fe<sub>2</sub>O<sub>3</sub> reduction reaction [45–47]. With the increase in temperature, the reduction of Fe<sub>2</sub>O<sub>3</sub> became more obvious. As the Fe<sub>2</sub>O<sub>3</sub> formed different types of oxides, it can be described by the following process:

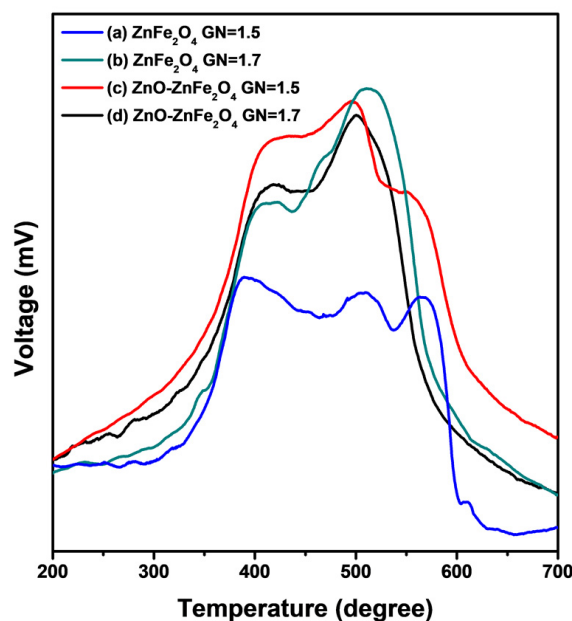


**Figure 11.** H<sub>2</sub>-TPR profiles of (a) ZnFe<sub>2</sub>O<sub>4</sub> (GN = 1.5), (b) ZnFe<sub>2</sub>O<sub>4</sub> (GN = 1.7), (c) ZnO-ZnFe<sub>2</sub>O<sub>4</sub> (GN = 1.5), and (d) ZnO-ZnFe<sub>2</sub>O<sub>4</sub> (GN = 1.7).

Fe<sub>2</sub>O<sub>3</sub> → Fe<sub>3</sub>O<sub>4</sub> was reduced at a low temperature of approximately 400 °C. The Fe<sub>2</sub>O<sub>3</sub> → FeO reduction occurred between 500 °C and 700 °C. Finally, FeO → Fe was reduced after 800 °C. On the other hand, the peak shift was also affected by the crystallinity and heating rate. If the crystallinity was stronger, the peak would shift to a higher temperature. As the heating rate increased, the peak would also shift to a higher temperature. In addition to the above factors, it can be seen from Figure 1 that the samples with a GN ratio of 1.7 demonstrated higher crystallinity. However, the peaks in Figure 11b,d shifted to a relatively lower temperature and formed a broad peak. As the samples with a GN ratio of 1.7 had a higher specific surface area and more pores than the samples with a GN ratio of 1.5, the samples could easily be reduced by hydrogen, which could correspond to the BET analysis and pore size distribution results (Table 1 and Figure 10e).

## 2.6. H<sub>2</sub> Production by the Steam Reforming of Methanol (SRM)

The H<sub>2</sub> generation rate was detected with a gas chromatograph. The hydrogen production was measured using a N<sub>2</sub> flow rate of 30 sccm in a temperature range of 350–500 °C. The H<sub>2</sub> production performance of the ZnFe<sub>2</sub>O<sub>4</sub> and ZnO-ZnFe<sub>2</sub>O<sub>4</sub> catalysts is mentioned in Table 2. It can be seen that as the temperature rose, the hydrogen production rate significantly improved. Table 2 lists the rate of H<sub>2</sub> production versus the reaction temperature of the ZnFe<sub>2</sub>O<sub>4</sub> and ZnO-ZnFe<sub>2</sub>O<sub>4</sub>. As shown in Table 2, the rate of the ZnO-ZnFe<sub>2</sub>O<sub>4</sub> at 500 °C could reach about 7300 mL STP min<sup>-1</sup> g-cat<sup>-1</sup> (G/N 1.5) and 7700 mL STP min<sup>-1</sup> g-cat<sup>-1</sup> (G/N 1.7). Figure 12 presents the H<sub>2</sub> production rates of the GNP-prepared ZnO-ZnFe<sub>2</sub>O<sub>4</sub> and ZnFe<sub>2</sub>O<sub>4</sub> powders; the CuCrO<sub>2</sub> bulk powder; the GNP-prepared CuCrO<sub>2</sub>, CuFeO<sub>2</sub>, and CuFeO<sub>2</sub>-CeO<sub>2</sub> nanopowders; and the commercial catalyst. According to the results, the catalytic performance of the ZnO-ZnFe<sub>2</sub>O<sub>4</sub> catalyst powders was higher than those of the aforementioned catalysts [48–50]. Due to the flammability and instability of hydrogen, SRM might entail some risks at high temperatures. From the H<sub>2</sub>-TPR studies, the ZnO-ZnFe<sub>2</sub>O<sub>4</sub> had thermal stability up to 500 °C. In addition, the process of preparing this powder is easy, cheap, and suitable for future commercial use.

**Table 2.** The rates of H<sub>2</sub> production at different temperatures in the SRM process for ZnFe<sub>2</sub>O<sub>4</sub> and ZnO-ZnFe<sub>2</sub>O<sub>4</sub> catalysts at a N<sub>2</sub> flow rate of 30 sccm.

Composition	Rate of H <sub>2</sub> Production (mL STP min <sup>-1</sup> g-cat <sup>-1</sup> )			
	350 °C	400 °C	450 °C	500 °C
ZnFe <sub>2</sub> O <sub>4</sub> (G/N 1.5)	1944	3881	6104	7023
ZnFe <sub>2</sub> O <sub>4</sub> (G/N 1.7)	2004	4342	6332	7260
ZnO-ZnFe <sub>2</sub> O <sub>4</sub> (G/N 1.5)	2174	4174	6484	7341
ZnO-ZnFe <sub>2</sub> O <sub>4</sub> (G/N 1.7)	2979	4391	6773	7745

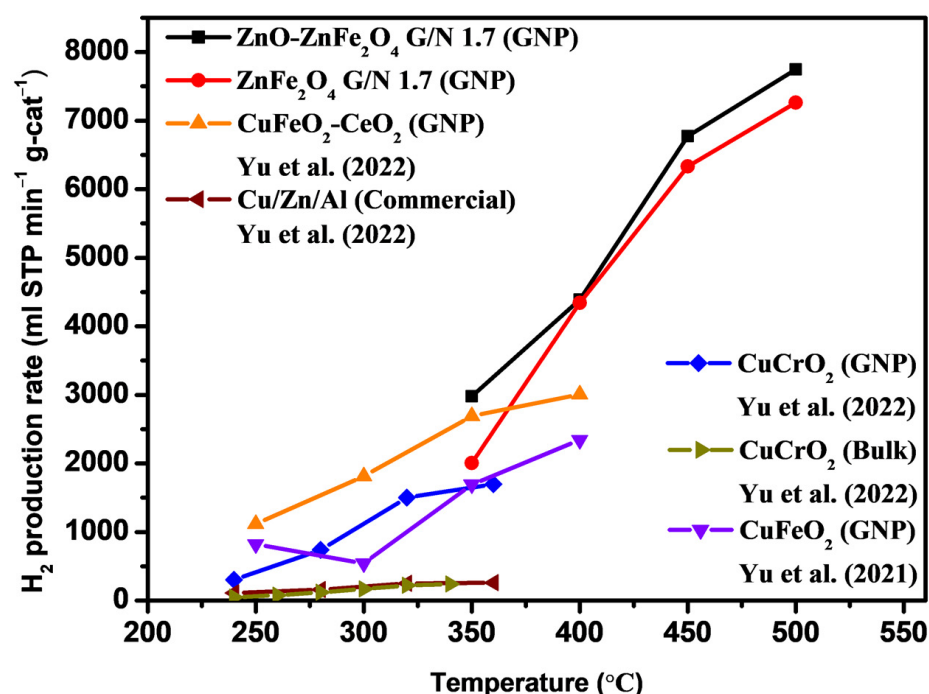


**Figure 12.** The H<sub>2</sub> production rates of the ZnFe<sub>2</sub>O<sub>4</sub> and ZnO-ZnFe<sub>2</sub>O<sub>4</sub> catalyst powders prepared by the GNP at a N<sub>2</sub> flow rate of 30 sccm in the SRM process and the H<sub>2</sub> production rates of CuCrO<sub>2</sub> bulk powder; the CuCrO<sub>2</sub>, CuFeO<sub>2</sub>, and CuFeO<sub>2</sub>-CeO<sub>2</sub> nanopowders prepared by the GNP; and a commercial catalyst [48–50].

### 2.7. Stability and Selectivity Studies

The stability of the catalyst was mainly affected by the formation of carbon coke. Therefore, reducing the generation of carbon coke could increase the stability of the catalyst. On the other hand, the precipitation of Zn, Fe, and ZnO particles improved their active sites and was also beneficial to the stability. To investigate the stability of the catalyst used in the SRM process, the ZnO-ZnFe<sub>2</sub>O<sub>4</sub> (GN = 1.7) catalyst had a long-term SRM process at 500 °C with a N<sub>2</sub> flow rate of 30 sccm for 168 h. As shown in Figure 13, it was found that the hydrogen production rate decreased by about 12% after the catalyst had operated for 168 h. This indicated that the ZnO-ZnFe<sub>2</sub>O<sub>4</sub> (GN = 1.7) catalyst had good catalytic stability.

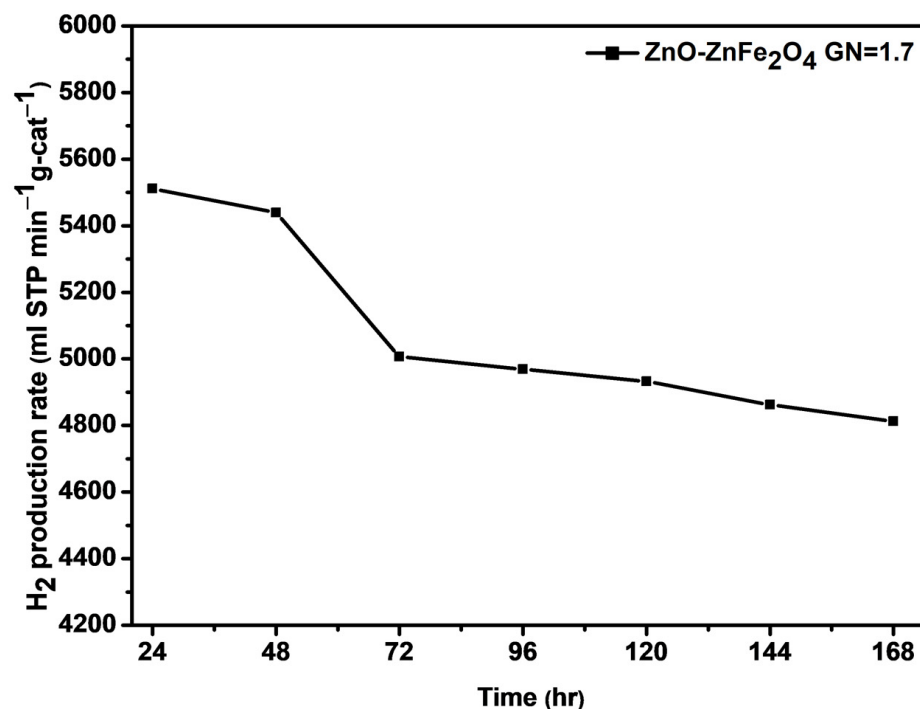


**Figure 13.** Long-term SRM process testing of ZnO-ZnFe<sub>2</sub>O<sub>4</sub> (GN = 1.7) catalyst at 500 °C with N<sub>2</sub> flow rate of 30 sccm for 168 h.

Due to methanol's high carbon-to-hydrogen ratio, SRM usually occurs at lower temperatures (200–300 °C) [51]. Therefore, when the temperature increases, the conversion rate of methanol will also be higher. When the temperature was higher than 300 °C, the methanol was completely converted [52]. Figure 14 shows the H<sub>2</sub>, CH<sub>4</sub>, CO, and CO<sub>2</sub> selectivity and conversion in the SRM process using the ZnO-ZnFe<sub>2</sub>O<sub>4</sub> (GN = 1.7) catalyst at 350–500 °C. Figure 14a shows that the selectivity of H<sub>2</sub> was the best in any temperature range, and there was a slight upward trend as the temperature increased. The conversion rate of H<sub>2</sub> also maintained a high conversion efficiency of more than 96% due to the presence of more active sites. The CH<sub>4</sub> generated H<sub>2</sub>, CO, and CO<sub>2</sub>. As can be seen in Figure 14b, the presence of CH<sub>4</sub> could be a consideration of the methanation of the CO and CO<sub>2</sub>. However, the CH<sub>4</sub> decreased when the reaction temperature increased, which was consistent with its subsequent conversion by steam reforming (reverse methanation reactions) at high temperatures. Figure 14c,d illustrate the relationship between temperature and carbon monoxide formation. As the temperature increased, the selectivity and quantity of CO also increased. This was consistent with the mechanism of the reverse water-gas shift displacement reaction to generate CO.

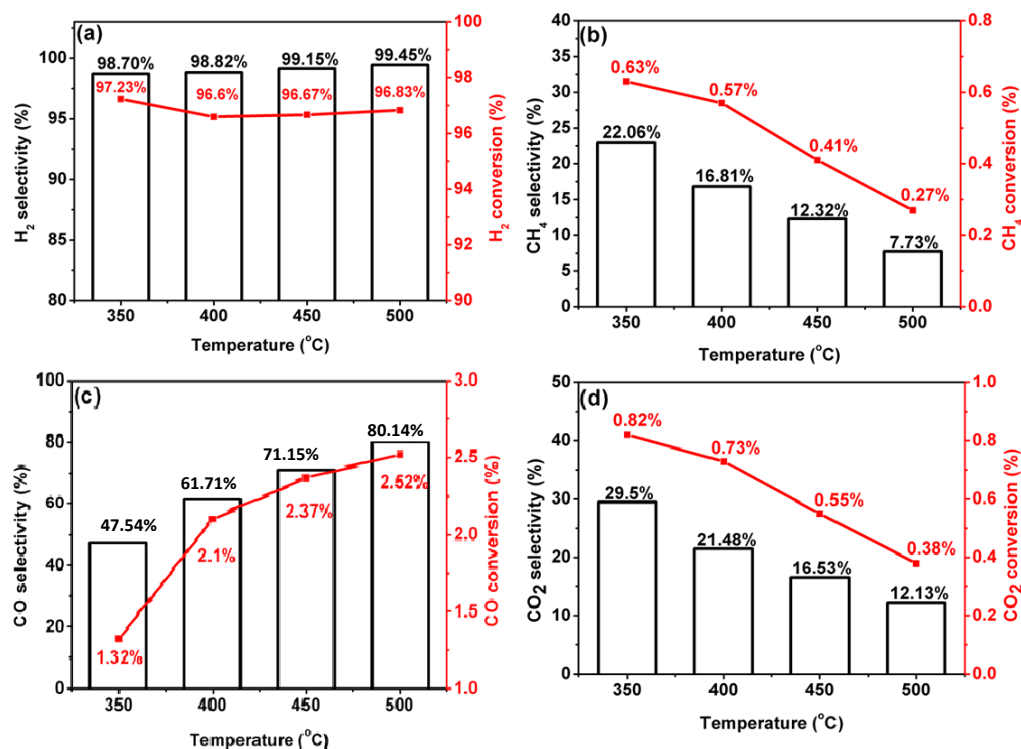


**Figure 14.** (a) H<sub>2</sub>, (b) CH<sub>4</sub>, (c) CO, and (d) CO<sub>2</sub> selectivity/conversion in the SRM process using the ZnO-ZnFe<sub>2</sub>O<sub>4</sub> (GN = 1.7) catalyst at 350–500 °C.

### 3. Materials and Methods

#### 3.1. Preparation of ZnFe<sub>2</sub>O<sub>4</sub> and ZnO-ZnFe<sub>2</sub>O<sub>4</sub> Catalysts

The ZnFe<sub>2</sub>O<sub>4</sub> and ZnO-ZnFe<sub>2</sub>O<sub>4</sub> catalysts were prepared through the GNP. The precursor was composed of zinc nitrate (99.0% purity, Aldrich AVATOR chemical company, Taiwan, China), ferric nitrate (99.0% purity, Aldrich AVATOR chemical company, Taiwan, China), glycine (99.9% purity, Aldrich AVATOR chemical company, Taiwan, China), and DI water. According to different atomic molar ratios (Zn: Fe = 1:2 or 1:1) and G/N molar ratios (nitrate: glycine = 1.5:1 or 1.7:1), the ZnFe<sub>2</sub>O<sub>4</sub> and ZnO-ZnFe<sub>2</sub>O<sub>4</sub> catalysts were dissolved in 5 mL of DI water. The precursor was then stirred on a hot plate at 80 °C for 20 h until the precursor was gelatinous. The precursor was then evaporated in an oven at 100 °C for 48 h until it was gel-like. Finally, the precursor was heated on a hot plate to 300 °C and combusted.

#### 3.2. Characterization Studies

The characterization of the ZnFe<sub>2</sub>O<sub>4</sub> and ZnO-ZnFe<sub>2</sub>O<sub>4</sub> catalyst powders was investigated by X-ray diffraction (XRD), a scanning electron microscope (SEM), a transmission electron microscope (TEM), and a Brunauer–Emmett–Teller (BET) analysis. After the H<sub>2</sub> production rate of the catalysts was estimated by gas chromatography (GC), the powders were characterized by XRD and SEM. Using a D2 Phaser (Bruker, Billerica, MA, USA), the crystal structures of the ZnFe<sub>2</sub>O<sub>4</sub> and ZnO-ZnFe<sub>2</sub>O<sub>4</sub> catalyst powders at a 2-theta angle of 20°–80° were analyzed with a working voltage of 30 kV under CuK $\alpha$  radiation ( $\lambda = 1.5418 \text{ \AA}$ ). The morphology of the catalysts was analyzed by field emission scanning electron microscopy (FESEM, Ultra-high Resolution Scanning Electron Microscope, SU8100, HITACHI, Tokyo, Japan) and transmission electron microscopy studies (TEM, JEOL JEM-2100F, Tokyo, Japan) with a working voltage of 200 kV. The elemental analysis was carried out using scanning transmission electron microscopy–energy dispersive X-ray spectroscopy (STEM-EDS) mapping. The specific surface area ( $S_{\text{BET}}$ ) was measured by a Micromeritics TriStar II plus analyzer (BET, Micromeritics Instrument Corporation, Norcross, GA, USA). The samples were degassed by passing high-purity nitrogen into the sample tube at 200 °C

for 2 h to remove excess water, and the sample was then placed in  $-196^{\circ}\text{C}$  liquid nitrogen. For the different relative pressures, the adsorption capacity of nitrogen was  $P/P_0 = 0-0.3$ .

### 3.3. Catalyst Test

The hydrogen production rates of the  $\text{ZnFe}_2\text{O}_4$  and  $\text{ZnO-ZnFe}_2\text{O}_4$  catalyst powders were analyzed with a GC equipped with a thermal conductivity detector (TCD). The gas from the outlet tube was analyzed using a gas chromatograph (GC 1000 China Chromatography TCD, New Taipei City, Taiwan) for each reaction temperature. The  $\text{H}_2$ -TPR was investigated with a Thermo Conductivity Analyzer (TCA 2004A, China Chromatography, New Taipei City, Taiwan); 20 mg of catalyst was placed in a tube furnace and heated to  $700^{\circ}\text{C}$  with  $\text{H}_2/\text{N}_2$  (10:90) mixed gas at a constant heating rate of  $10^{\circ}\text{C}/\text{min}$ . The SRM reaction was carried out in a tubular flow reactor with a 25 cm quartz tube with an inner diameter of 1.2 cm, and nitrogen was used as the carrier gas at a flow rate of 30 sccm. The amount of catalyst metal used for the reaction was 20 mg. The system was connected with a gas chromatograph equipped with a thermal conductivity detector ( $\text{H}_2$ ,  $\text{CO}$ ,  $\text{CO}_2$ , and  $\text{CH}_4$ ). The methanol and steam feed was produced with a mixture of methanol and water in a 3:1 molar ratio. It vaporized by heating to  $80^{\circ}\text{C}$ , after which the methanol and steam feed was carried by the nitrogen flow. The as-prepared powder samples were mounted in the middle of a quartz tube with quartz cotton and heated to  $350^{\circ}\text{C}$ ,  $400^{\circ}\text{C}$ ,  $450^{\circ}\text{C}$ , and  $500^{\circ}\text{C}$ , respectively. The gas from the outlet tube was analyzed with a gas chromatograph at each temperature several times and was averaged [32,52]. The following definitions were used to describe the SRM performance parameters:

$$\text{Methanol conversion (\%)} = \frac{(\text{methanol})_{in} - (\text{methanol})_{out}}{(\text{methanol})_{in}} \times 100 \quad (9)$$

$$\text{Hydrogen production rate} = \frac{\text{H}_2 \times \text{rate of flow}}{\text{Vol/mass (cat)}} \quad (10)$$

$$X \text{ (X = H}_2, \text{CO, CO}_2 \text{ or CH}_4\text{) Selectivity (\%)} = \frac{X}{(\text{H}_2 + \text{CO} + \text{CO}_2 + \text{CH}_4)} \times 100 \quad (11)$$

$$\text{H}_2 \text{ Selectivity (\%)} = \frac{\text{H}_2}{(\text{H}_2 + \text{CH}_4)} \times 100 \quad (12)$$

$$\text{CO Selectivity (\%)} = \frac{\text{CO}}{(\text{CO} + \text{CO}_2 + \text{CH}_4)} \times 100 \quad (13)$$

$$\text{CO}_2 \text{ Selectivity (\%)} = \frac{\text{CO}_2}{(\text{CO} + \text{CO}_2 + \text{CH}_4)} \times 100 \quad (14)$$

$$\text{CH}_4 \text{ Selectivity (\%)} = \frac{\text{CH}_4}{(\text{CO} + \text{CO}_2 + \text{CH}_4)} \times 100 \quad (15)$$

## 4. Conclusions

In this experiment,  $\text{ZnFe}_2\text{O}_4$  and  $\text{ZnO-ZnFe}_2\text{O}_4$  catalyst powders (G/N = 1.5, 1.7) were successfully prepared and used as a catalyst in the SRM process. The crystal phases of the  $\text{ZnFe}_2\text{O}_4$  and  $\text{ZnO-ZnFe}_2\text{O}_4$  were determined by XRD diffraction. The surface structures, interplanar spacings, and diffraction patterns of the powders were observed using a scanning electron microscope and a transmission electron microscope. The surface area and adsorption-desorption mode of the catalyst powder were then measured using a Brunauer-Emmett-Teller analysis. The specific surface area of the  $\text{ZnFe}_2\text{O}_4$  and  $\text{ZnO-ZnFe}_2\text{O}_4$  catalysts varied from  $5.66 \text{ m}^2/\text{g}$  to  $11.67 \text{ m}^2/\text{g}$ . Moreover, the  $\text{ZnO-ZnFe}_2\text{O}_4$  (G/N = 1.5) had better dispersibility due to the presence of ZnO; therefore, it had a higher surface area than the  $\text{ZnFe}_2\text{O}_4$  (G/N = 1.5). The  $\text{ZnO-ZnFe}_2\text{O}_4$  (G/N 1.7) catalyst had the best hydrogen

production rate of 7745 mL STP min<sup>-1</sup> g-cat<sup>-1</sup> at 500 °C. The ZnO incorporation improved the specific surface area of the ZnO-ZnFe<sub>2</sub>O<sub>4</sub> (G/N 1.7) catalyst. The simple preparation process of the ZnFe<sub>2</sub>O<sub>4</sub> and ZnO-ZnFe<sub>2</sub>O<sub>4</sub> catalyst powders demonstrated good catalytic activity. These catalysts provided the best H<sub>2</sub> production efficiency in SRM reactions at different ranges of temperature. Based on these studies, SRM will gradually become a feasible method for producing hydrogen as an alternative energy source in industry.

**Author Contributions:** Conceptualization, B.-Z.H., C.-L.Y., S.S. and T.-W.C.; methodology, B.-Z.H., C.-L.Y. and B.-S.Y.; software, C.-L.Y. and S.S.; validation, T.-W.C., B.-S.Y., C.-C.L. and L.F.; formal analysis, C.-L.Y., S.S. and T.-W.C.; investigation, B.-Z.H., C.-L.Y. and T.-W.C.; resources, T.-W.C. and L.F.; data curation, B.-Z.H., C.-L.Y., B.-S.Y., C.-C.L., L.F. and Y.-H.L.; writing—original draft preparation, B.-Z.H., C.-L.Y., S.S. and T.-W.C.; writing—review and editing, B.-Z.H., C.-L.Y., S.S., T.-W.C., B.-S.Y., C.-C.L., L.F. and Y.-H.L.; visualization, B.-Z.H. and C.-L.Y.; supervision, T.-W.C. and L.F.; project administration T.-W.C.; funding acquisition T.-W.C. and L.F. All authors have read and agreed to the published version of the manuscript.

**Funding:** This work was supported by the Ministry of Science and Technology of Taiwan (MOST 108-2221-E-027-056, MOST 109-2221-E-027-068, MOST 109-2221-E-027-059, and MOST 109-2113-M-027-001-MY3, MOST 110-2221-E-027-041). This work was supported by the National Science and Technology Council of Taiwan (NSTC 111-2221-E-027-104). This work was supported by the University System of Taipei Joint Research Program (NTUT-SZU-112-06). The authors appreciate the Precision Research and Analysis Centre of the National Taipei University of Technology (NTUT) for providing the measurement facilities.

**Data Availability Statement:** The data are contained within the article.

**Conflicts of Interest:** The authors declare no conflict of interest.

## References

1. Armaroli, N.; Balzani, V. The Future of Energy Supply: Challenges and Opportunities. *Angew. Chem. Int. Ed.* **2007**, *46*, 52–66. [[CrossRef](#)]
2. Bistline, J.; Bragg-Sitton, S.; Cole, W.; Dixon, B.; Eschmann, E.; Ho, J.; Kwon, A.; Martin, L.; Murphy, C.; Namovicz, C.; et al. Modeling Nuclear Energy's Future Role in Decarbonized Energy Systems. *iScience* **2023**, *26*, 105952. [[CrossRef](#)]
3. Basile, A.; Parmaliana, A.; Tosti, S.; Iulianelli, A.; Gallucci, F.; Espro, C.; Spooen, J. Hydrogen Production by Methanol Steam Reforming Carried Out in Membrane Reactor on Cu/Zn/Mg-Based Catalyst. *Catal. Today* **2008**, *137*, 17–22. [[CrossRef](#)]
4. Zhang, R.; Huang, C.; Zong, L.; Lu, K.; Wang, X.; Cai, J. Hydrogen Production from Methanol Steam Reforming over TiO<sub>2</sub> and CeO<sub>2</sub> Pillared Clay Supported Au Catalysts. *Appl. Sci.* **2018**, *8*, 176. [[CrossRef](#)]
5. Kannan, N.; Vakeesan, D. Solar Energy for Future World: A Review. *Renew. Sustain. Energy Rev.* **2016**, *62*, 1092–1105. [[CrossRef](#)]
6. Joselin Herbert, G.M.; Iniyar, S.; Sreevalsan, E.; Rajapandian, S. A Review of Wind Energy Technologies. *Renew. Sustain. Energy Rev.* **2007**, *11*, 1117–1145. [[CrossRef](#)]
7. Shanmugam, V.; Neuberg, S.; Zapf, R.; Pennemann, H.; Kolb, G. Hydrogen Production over Highly Active Pt Based Catalyst Coatings by Steam Reforming of Methanol: Effect of Support and Co-Support. *Int. J. Hydrogen Energy* **2019**, *45*, 1658–1670. [[CrossRef](#)]
8. Palo, D.R.; Dagle, R.A.; Holladay, J.D. Methanol Steam Reforming for Hydrogen Production. *Chem. Rev.* **2007**, *107*, 3992–4021. [[CrossRef](#)] [[PubMed](#)]
9. Velu, S.; Suzuki, K.; Kapoor, M.P.; Ohashi, F.; Osaki, T. Selective Production of Hydrogen for Fuel Cells via Oxidative Steam Reforming of Methanol over CuZnAl(Zr)-Oxide Catalysts. *Appl. Catal. Gen.* **2001**, *213*, 47–63. [[CrossRef](#)]
10. Hwang, B.Y.; Sakthinathan, S.; Chiu, T.W. Production of Hydrogen from Steam Reforming of Methanol Carried out by Self-Combusted CuCr<sub>1-x</sub>Fe<sub>x</sub>O<sub>2</sub> (x = 0–1) Nanopowders Catalyst. *Int. J. Hydrogen Energy* **2019**, *44*, 2848–2856. [[CrossRef](#)]
11. Chiu, T.W.; Hong, R.T.; Yu, B.S.; Huang, Y.H.; Kameoka, S.; Tsai, A.P. Improving Steam-Reforming Performance by Nanopowdering CuCrO<sub>2</sub>. *Int. J. Hydrogen Energy* **2014**, *39*, 14222–14226. [[CrossRef](#)]
12. Wang, S.F.; Lu, C.M.; Wu, Y.C.; Yang, Y.C.; Chiu, T.W. La<sub>2</sub>O<sub>3</sub>-Al<sub>2</sub>O<sub>3</sub>-B<sub>2</sub>O<sub>3</sub>-SiO<sub>2</sub> Glasses for Solid Oxide Fuel Cell Applications. *Int. J. Hydrogen Energy* **2011**, *36*, 3666–3672. [[CrossRef](#)]
13. Hsu, K.C.; Yu, C.L.; Lei, H.J.; Sakthinathan, S.; Chen, P.C.; Lin, C.C.; Chiu, T.W.; Nagaraj, K.; Fan, L.; Lee, Y.H. Modification of Electrospun CeO<sub>2</sub> Nanofibers with CuCrO<sub>2</sub> Particles Applied to Hydrogen Harvest from Steam Reforming of Methanol. *Materials* **2022**, *15*, 8770. [[CrossRef](#)] [[PubMed](#)]
14. Hsu, K.C.; Keyan, A.K.; Hung, C.W.; Sakthinathan, S.; Yu, C.L.; Chiu, T.W.; Nagaraj, K.; Fan, F.Y.; Shan, Y.K.; Chen, P.C. Fabrication of CuYO<sub>2</sub> Nanofibers by Electrospinning and Applied to Hydrogen Harvest. *Materials* **2022**, *15*, 8957. [[CrossRef](#)]
15. Kameoka, S.; Tanabe, T.; Tsai, A.P. Self-Assembled Porous Nano-Composite with High Catalytic Performance by Reduction of Tetragonal Spinel CuFe<sub>2</sub>O<sub>4</sub>. *Appl. Catal. Gen.* **2010**, *375*, 163–171. [[CrossRef](#)]

16. Asprey, S.P.; Wojciechowski, B.W.; Peppley, B.A. Kinetic Studies Using Temperature-Canning: The Steam-Reforming of Methanol. *Appl. Catal. Gen.* **1999**, *179*, 51–70. [[CrossRef](#)]
17. Mastalir, A.; Frank, B.; Szizybalski, A.; Soerijanto, H.; Deshpande, A.; Niederberger, M.; Schomäcker, R.; Schlögl, R.; Ressler, T. Steam Reforming of Methanol over Cu/ZrO<sub>2</sub>/CeO<sub>2</sub> Catalysts: A Kinetic Study. *J. Catal.* **2005**, *230*, 464–475. [[CrossRef](#)]
18. Sun, Z.; Zhang, X.; Li, H.; Liu, T.; Sang, S.; Chen, S.; Duan, L.; Zeng, L.; Xiang, W.; Gong, J. Chemical Looping Oxidative Steam Reforming of Methanol: A New Pathway for Auto-Thermal Conversion. *Appl. Catal. Environ.* **2020**, *269*, 118758. [[CrossRef](#)]
19. Li, H.; Tian, H.; Chen, S.; Sun, Z.; Liu, T.; Liu, R.; Assabumrungrat, S.; Saupsor, J.; Mu, R.; Pei, C.; et al. Sorption Enhanced Steam Reforming of Methanol for High-Purity Hydrogen Production over Cu-MgO/Al<sub>2</sub>O<sub>3</sub> Bifunctional Catalysts. *Appl. Catal. Environ.* **2020**, *276*, 119052. [[CrossRef](#)]
20. Khani, Y.; Bahadoran, F.; Safari, N.; Soltanali, S.; Taheri, S.A. Hydrogen Production from Steam Reforming of Methanol over Cu-Based Catalysts: The Behavior of Zn<sub>x</sub>La<sub>x</sub>Al<sub>1-x</sub>O<sub>4</sub> and ZnO/La<sub>2</sub>O<sub>3</sub>/Al<sub>2</sub>O<sub>3</sub> Lined on Cordierite Monolith Reactors. *Int. J. Hydrogen Energy* **2019**, *44*, 11824–11837. [[CrossRef](#)]
21. Garbarino, G.; Pugliese, F.; Cavattoni, T.; Busca, G.; Costamagna, P. A Study on CO<sub>2</sub> Methanation and Steam Methane Reforming over Commercial Ni/Calcium Aluminate Catalysts. *Energies* **2020**, *13*, 2792. [[CrossRef](#)]
22. Perry, R.H.; Green, D.W. *Perrys Chemical Engineers Handbook*, 8th ed.; McGraw-Hill: New York, NY, USA, 2008.
23. Shen, J.P.; Song, C. Influence of Preparation Method on Performance of Cu/Zn-Based Catalysts for Low-Temperature Steam Reforming and Oxidative Steam Reforming of Methanol for H<sub>2</sub> Production for Fuel Cells. *Catal. Today* **2002**, *77*, 89–98. [[CrossRef](#)]
24. Agrell, J.; Birgersson, H.; Boutonnet, M. Steam Reforming of Methanol over a Cu/ZnO/Al<sub>2</sub>O<sub>3</sub> Catalyst: A Kinetic Analysis and Strategies for Suppression of CO Formation. *J. Power Source* **2002**, *106*, 249–257. [[CrossRef](#)]
25. Shishido, T.; Yamamoto, Y.; Morioka, H.; Takaki, K.; Takehira, K. Active Cu/ZnO and Cu/ZnO/Al<sub>2</sub>O<sub>3</sub> Catalysts Prepared by Homogeneous Precipitation Method in Steam Reforming of Methanol. *Appl. Catal. Gen.* **2004**, *263*, 249–253. [[CrossRef](#)]
26. Szizybalski, A.; Girgsdies, F.; Rabis, A.; Wang, Y.; Niederberger, M.; Ressler, T. In Situ Investigations of Structure-Activity Relationships of a Cu/ZrO<sub>2</sub> Catalyst for The Steam Reforming of Methanol. *J. Catal.* **2005**, *233*, 297–307. [[CrossRef](#)]
27. Huang, G.; Liaw, B.J.; Jhang, C.J.; Chen, Y.Z. Steam Reforming of Methanol over CuO/ZnO/CeO<sub>2</sub>/ZrO<sub>2</sub>/Al<sub>2</sub>O<sub>3</sub> Catalysts. *Appl. Catal. A Gen.* **2009**, *358*, 7–12. [[CrossRef](#)]
28. Sun, Y.; Chen, L.; Bao, Y.; Zhang, Y.; Wang, J.; Fu, M.; Wu, J.; Ye, D. The Applications of Morphology Controlled ZnO in Catalysis. *Catalysts* **2016**, *6*, 188. [[CrossRef](#)]
29. Pipitone, G.; Zoppi, G.; Pirone, R.; Bensaid, S. A critical Review on Catalyst Design for Aqueous Phase Reforming. *Int. J. Hydrogen Energy* **2022**, *47*, 151–180. [[CrossRef](#)]
30. Zoppi, G.; Pipitone, G.; Pirone, R.; Bensaid, S. Aqueous Phase Reforming Process for The Valorization of Wastewater Streams: Application to Different Industrial Scenarios. *Catal. Today* **2022**, *387*, 224–236. [[CrossRef](#)]
31. Huang, R.J.; Sakthinathan, S.; Chiu, T.W.; Dong, C. Hydrothermal Synthesis of High Surface Area CuCrO<sub>2</sub> for H<sub>2</sub> Production by Methanol Steam Reforming. *RSC Adv.* **2021**, *11*, 12607–12613. [[CrossRef](#)]
32. Yu, C.L.; Sakthinathan, S.; Hwang, B.Y.; Lin, S.Y.; Chiu, T.W.; Yu, B.S.; Fan, Y.J.; Chuang, C. CuFeO<sub>2</sub>-CeO<sub>2</sub> Nanopowder Catalyst Prepared by Self-Combustion Glycine Nitrate Process and Applied for Hydrogen Production from Methanol Steam Reforming. *Int. J. Hydrogen Energy* **2020**, *45*, 15752–15762. [[CrossRef](#)]
33. Yang, M.; Li, S.; Chen, G. High-Temperature Steam Reforming of Methanol over ZnO-Al<sub>2</sub>O<sub>3</sub> Catalysts. *Appl. Catal. Environ.* **2011**, *101*, 409–416. [[CrossRef](#)]
34. Mao, N. Investigating the Heterojunction between ZnO/Fe<sub>2</sub>O<sub>3</sub> and g-C<sub>3</sub>N<sub>4</sub> for An Enhanced Photocatalytic H<sub>2</sub> Production under Visible-Light Irradiation. *Sci. Rep.* **2019**, *9*, 12383. [[CrossRef](#)] [[PubMed](#)]
35. Wu, Y.; Zeng, S.; Dong, Y.; Fu, Y.; Sun, H.; Yin, S.; Guo, X.; Qin, W. Hydrogen Production from Methanol Aqueous Solution by ZnO/Zn(OH)<sub>2</sub> Macrostructure Photocatalysts. *RSC Adv.* **2018**, *8*, 11395–11402. [[CrossRef](#)]
36. Perez, Y.P.; Martinez, O.A.; Pena, P.A.; Vargas, C.E.S.; Ruiz, S.O.; Hernandez, F.G.; Gomez, R.; Tzompantzi, F. Novel ZnS-ZnO Composite Synthesized by The Solvothermal Method through The Partial Sulfidation of ZnO for H<sub>2</sub> Production without Sacrificial Agent. *Appl. Catal. Environ.* **2018**, *230*, 125–134. [[CrossRef](#)]
37. Dhanalakshmi, A.; Natarajan, B.; Ramadas, V.; Palanimurugan, A. Thanikaikarasan, Structural, Morphological, Optical and Antibacterial Activity of Rod-Shaped Zinc Oxide and Manganese-Doped Zinc Oxide Nanoparticles. *Pramana J. Phys.* **2016**, *87*, 57. [[CrossRef](#)]
38. Sahoo, G.P.; Samanta, S.; Bhui, D.K.; Pyne, S.; Maity, A.; Misra, A. Hydrothermal Synthesis of Hexagonal ZnO Microstructures in HPMC Polymer Matrix and Their Catalytic Activities. *J. Mol. Liq.* **2015**, *212*, 665–670. [[CrossRef](#)]
39. Kiran, S.; Saibaba, K.; Ramesh, T.; Ashok, K.; Polu, A.R. Preparation and Characterization of ZnO-ZnFe<sub>2</sub>O<sub>4</sub> Nanocomposites. *Macromol. Symp.* **2023**, *407*, 2200027. [[CrossRef](#)]
40. AlSalhi, M.S.; Devanesan, S.; Asemi, N.; Ahamed, A. Concurrent Fabrication of ZnO-ZnFe<sub>2</sub>O<sub>4</sub> Hybrid Nanocomposite for Enhancing Photocatalytic Degradation of Organic Pollutants and Its Bacterial Inactivation. *Chemosphere* **2023**, *318*, 137928. [[CrossRef](#)]
41. Xu, Y.; Wu, S.; Li, X.; Huang, Y.; Wang, Z.; Han, Y.; Wu, J.; Meng, H.; Zhang, X. Synthesis, Characterization, and Photocatalytic Degradation Properties of ZnO/ZnFe<sub>2</sub>O<sub>4</sub> Magnetic Heterostructures. *New J. Chem.* **2017**, *41*, 15433–15438. [[CrossRef](#)]
42. Liu, T.; Xu, D.; Wu, D.; Liu, G.; Hong, X. Spinel ZnFe<sub>2</sub>O<sub>4</sub> Regulates Copper Sites for CO<sub>2</sub> Hydrogenation to Methanol. *ACS Sustain. Chem. Eng.* **2021**, *9*, 4033–4041. [[CrossRef](#)]

43. Wang, L.; Gao, X.; Bai, Y.; Tan, M.; Sun, K.; Zhang, T.; Wu, Y.; Pan, J.; Xie, H.; Tan, Y. The Synergistic Effect Between ZnO and ZnCr<sub>2</sub>O<sub>4</sub> on The Catalytic Performance for Isobutanol Synthesis from Syngas. *Fuel* **2019**, *253*, 1570–1577. [[CrossRef](#)]
44. Wen, J.; Guo, H.; Ma, X.; Wei, Z.; He, X.; Zhang, L.; Li, B.; Wang, T.; Cheng, Y. Mesoporous Ce-Doped ZnO Hollow Microspheres for Oxidation of 1,2-dichlorobenzene. *Catal. Sci. Technol.* **2020**, *10*, 3739–3747. [[CrossRef](#)]
45. Liang, M.; Kang, W.; Xie, K. Comparison of Reduction Behavior of Fe<sub>2</sub>O<sub>3</sub>, ZnO and ZnFe<sub>2</sub>O<sub>4</sub> by TPR Technique. *J. Nat. Gas Chem.* **2009**, *18*, 110–113. [[CrossRef](#)]
46. Papa, F.; Patron, L.; Carp, O.; Paraschiv, C.; Balint, I. Catalytic Behaviour of Neodymium Substituted Zinc Ferrites in Oxidative Coupling of Methane. *Rev. Roum. Chim.* **2010**, *55*, 33–38.
47. Munteanu, G.; Ilieva, L.; Andreeva, D. Kinetic Parameters Obtained from TPR Data for  $\alpha$ -Fe<sub>2</sub>O<sub>3</sub> and Au/ $\alpha$ -Fe<sub>2</sub>O<sub>3</sub> Systems. *Thermochim. Acta* **1997**, *291*, 171–177. [[CrossRef](#)]
48. Yu, C.L.; Sakthinathan, S.; Chen, S.Y.; Yu, B.S.; Chiu, T.W.; Dong, C. Hydrogen Generation by Methanol Steam Reforming Process by Delafossite-Type CuYO<sub>2</sub> Nanopowder Catalyst. *Micropor. Mesopor. Mat.* **2021**, *324*, 111305. [[CrossRef](#)]
49. Yu, C.L.; Lai, G.T.; Sakthinathan, S.; Lin, C.C.; Chiu, T.W.; Liu, M.C. Hydrogen Generation from Methanol Steam Reforming Process of CuCrO<sub>2</sub>-CeO<sub>2</sub> Nanopowders Catalyst. *Mater. Sci. Eng.* **2022**, *286*, 115989. [[CrossRef](#)]
50. Yu, C.L.; Sakthinathan, S.; Lai, G.T.; Lin, C.C.; Chiu, T.W.; Liu, M.C. ZnO-ZnCr<sub>2</sub>O<sub>4</sub> Composite Prepared by A Glycine Nitrate Process Method and Applied for Hydrogen Production by Steam Reforming of Methanol. *RSC Adv.* **2022**, *12*, 22097–22107. [[CrossRef](#)]
51. Bepari, S.; Kuila, D. Steam Reforming of Methanol, Ethanol, and Glycerol over Nickel-Based Catalysts-A Review. *Int. J. Hydrogen Energy* **2019**, *45*, 18090–18113. [[CrossRef](#)]
52. Tahay, P.; Khani, Y.; Jabari, M. Synthesis of Cubic and Hexagonal ZnTiO<sub>3</sub> as Catalyst Support in Steam Reforming of Methanol: Study of Physical and Chemical Properties of Copper Catalysts on The H<sub>2</sub> and CO Selectivity and Coke Formation. *Int. J. Hydrogen Energy* **2020**, *45*, 9484–9495. [[CrossRef](#)]

**Disclaimer/Publisher's Note:** The statements, opinions and data contained in all publications are solely those of the individual author(s) and contributor(s) and not of MDPI and/or the editor(s). MDPI and/or the editor(s) disclaim responsibility for any injury to people or property resulting from any ideas, methods, instructions or products referred to in the content.